Hybrid AC/DC Collection and HVDC Transmission Topology for Large-scale Offshore Wind Farms

Wang Xiang, *Senior Member*, *IEEE*, *Member*, *CSEE*, Rui Tu, Mingyu Han, and Jinyu Wen, *Senior Member*, *IEEE*, *Fellow*, *CSEE*

***Abstract*—Conventional offshore wind integration systems use 33kV or 66kV AC cables to collect wind energy and employ high voltage direct current (HVDC) transmission technology to deliver wind power to onshore grids. This scheme suffers from high costs for collection systems and offshore platforms when the capacity of offshore wind farms increases. This paper proposes a hybrid AC/DC collection and HVDC transmission concept for the large-scale offshore wind integration system. Wind farms near the offshore converter platform are integrated using AC collection cables, while the remaining wind farms are integrated using DC collection cables. The AC and DC collection cables infeed to the offshore converter platform, which features a three-terminal hybrid AC/DC/DC hub. The system layout and operating principle of the hybrid AC/DC collection and HVDC transmission system are introduced in detail. The control strategy and parameter design of the hybrid AC/DC/DC hub are presented. An economic evaluation comparing conventional AC collection and HVDC transmission schemes is conducted. It is indicated that the proposed integration concept can reduce the operating power capacity and power loss of the offshore converter, enhancing the economic efficiency of the overall integration system. Finally, the effectiveness of the proposed integration technology is validated in a 2000MW offshore wind power integration system by PSCAD/EMTDC simulation analysis.**

***Index Terms*—HVDC converter, HVDC transmission, hybrid collection, offshore wind integration, wind energy.**

I. Introduction

THE utilization of offshore wind power is an important approach to promoting green energy transition. According to the Global Wind Energy Council, 130 GW offshore wind is expected to be installed worldwide in 2023–2027, with an average annual installation of nearly 26 GW [1].

For remote offshore wind integration, HVDC transmission based on modular multilevel converters (MMCs) has been widely acknowledged as a feasible technical solution [2]. Compared with HVAC transmission, HVDC transmission provides unlimited transmission distance, larger capacity, and lower operating loss. However, with the increase in offshore wind farm capacity, the cost of offshore platforms will increase significantly. To reduce the cost of offshore step-up transformer platforms, Borwin 5–6 and Dogger bank projects use 66 kV AC cables to directly connect offshore wind farms to the offshore converter platform. Reference [3] compares the economy of the two collection schemes. It is pointed out that removing the 33 kV/220 kV step-up transformer platforms saves the cost by 15%. Nevertheless, with the increasing scale of offshore wind farms, the total length of the AC collection network will be hundreds of kilometers, resulting in large reactive charging currents, high operating power loss and high cost [4].

To reduce the collection network cost, references [5] and [6] proposed DC collection and HVDC transmission technology for offshore wind farms. In early studies, DC collection approaches can be categorized into series and parallel structures of DC wind farms [7]–[9]. The series structure raises the DC collection voltage by implementing DC wind turbines (WTs) in serial connection [10]. However, the DC WTs close to high-voltage collection cables should withstand high insulation requirements. The parallel structure provides high operation ability but needs to construct a high-ratio offshore DC/DC converter station for cascade voltage boost [11], [12].

Various high-power DC/DC converters have been proposed to connect the medium voltage DC (MVDC) collection system with the HVDC transmission system, including the modular isolated LLC DC/DC converter [13], the modular dual-active-bridge (DAB) isolated DC-DC converter [14], and the thyristor-based modular DC/DC converter [15]. Additionally, to avoid the construction of the offshore DC/DC converter platform, [16] introduced a modular isolated DAB DC-DC converter-based series-connected offshore wind farm, where the DAB converter is installed in the nacelle of WTs. However, the insulation issues for the DAB converters close to high-voltage collection cables still exist. The conversion efficiency of DAB is generally restricted due to high turn-off loss. References [17], [18] proposed the multi-functional DC collector for all-DC offshore wind power systems, envisaging centralized and grouped configurations of DC collectors. However, when the transmission capacity is large, the number of cascaded SMs becomes very large, leading to high control complexity and low reliability. Notably, the aforementioned approaches

Manuscript received July 18, 2024; revised October 10, 2024; accepted November 14, 2024. Date of online publication January 10, 2025; date of current version March 21, 2025. This work was supported by the National Key Research and Development Program of China (2022YFB2405400), in part by the National Natural Science Foundation of China (52237004).

W. Xiang (corresponding author, email: xiangwang1003@foxmail.com; ORCID: https://orcid.org/0000-0002-4619-5849), R. Tu and J. Y. Wen are with the School of Electrical and Electronic Engineering, Huazhong University of Science and Technology, Wuhan 430074, China, and also with the State Key Laboratory of Advanced Electromagnetic Technology, Huazhong University of Science and Technology, Wuhan 430074, China.

M. Y. Han is with the Changzhou Power Supply Company of State Grid Jiangsu Electric Power Co., Ltd., Changzhou 213000, China.

DOI: 10.17775/CSEEJPES.2024.05450

did not test the feasibility of large-scale offshore wind farms, i.e., 2000 MW and above.

This paper proposes a hybrid AC/DC collection and HVDC transmission concept for large-scale offshore wind farms to address these challenges. Wind farms near the offshore converter platform are integrated using AC collection cables, while wind farms in distant locations utilize DC collection cables. The main contributions of this paper are as follows:

- A hybrid AC/DC collection and HVDC transmission topology for large-scale offshore wind farms is proposed, offering lower operating power loss and reduced investment costs compared to existing integration technologies.
- A design method for the DC voltage and power ratios of the hybrid AC/DC collection and HVDC transmission system is presented, ensuring maximum operating efficiency for the AC/DC/DC hub.
- Two control strategies for the AC/DC/DC hub are proposed. Both can provide sound grid-forming capabilities for AC and DC wind farms.

The remainder of this paper is organized as follows. Section II depicts the topology and operating principle of the hybrid AC/DC collection and HVDC transmission system. Section III details the parameters of the system's design. Section IV presents two AC/DC/DC hub control strategies. In Section V, the economic evaluation of the proposed topology is conducted. Simulation verifications of the proposed topology under normal operation, power curtailment and single-type WF operations are provided in Section VI. Finally, conclusions are drawn in Section VII.

II. Topology of Hybrid AC/DC Collection and HVDC Transmission System

A. Topology Structure

The topology of the hybrid AC/DC collection and HVDC transmission system for large-scale offshore wind farms is shown in Fig. 1. It mainly consists of offshore DC wind farms, DC collection network, offshore AC wind farms, AC collection network, offshore three-port AC/DC/DC hub, HVDC submarine cables and onshore MMC station.

Given that the large-scale wind farms occupy a large sea area, the wind farms close to the offshore converter platform are integrated using AC collection cables, while the remaining remote wind farms are integrated using DC collection cables. In the proposed integration system, the AC wind farms are collected directly to the point of common coupling (PCC) via the 66 kV AC collection cables and connected to the AC port of the AC/DC/DC hub. The DC wind farms use multiple DC WTs in series and parallel connections to form a group of WT clusters. The clusters are connected directly to the DC ports of the AC/DC/DC hub through MVDC collection cables. Then, the wind power is delivered to the onshore MMC station through the HVDC submarine cables.

The AC WTs adopt direct-drive permanent magnet synchronous generators (PMSG), while the DC WTs are modified from a PMSG by connecting an AC/DC converter [17]. All offshore wind farms use high-capacity WTs with a rated capacity of 10 MW. The output voltage of AC WTs is boosted from 3.15 kV to 66 kV. The output voltage of DC WTs is $\pm$ 20 kV.

The AC/DC/DC hub is the key equipment used in the proposed integration system. Its topology is shown in the red dashed box in Fig. 1. It mainly consists of three MMCs in parallel connection at the AC terminals and a series connection at the HVDC terminal. The AC/DC/DC hub contains a DC input port, an AC input port and a DC output port. The DC input port is connected with the MVDC collection network through the DC terminal of MMC2. The AC input port is connected with the 66 kV AC collection network through AC terminals of MMC1-MMC3. Then, the total wind power is transmitted via the DC output port.

B. Operating Principle

Denote the transmitted power of the DC wind farms as P_{dcwf} and the power of the AC wind farms as P_{acwf}. The DC output voltages of MMC1-MMC3 are V_{MMC1}, V_{MMC2} and

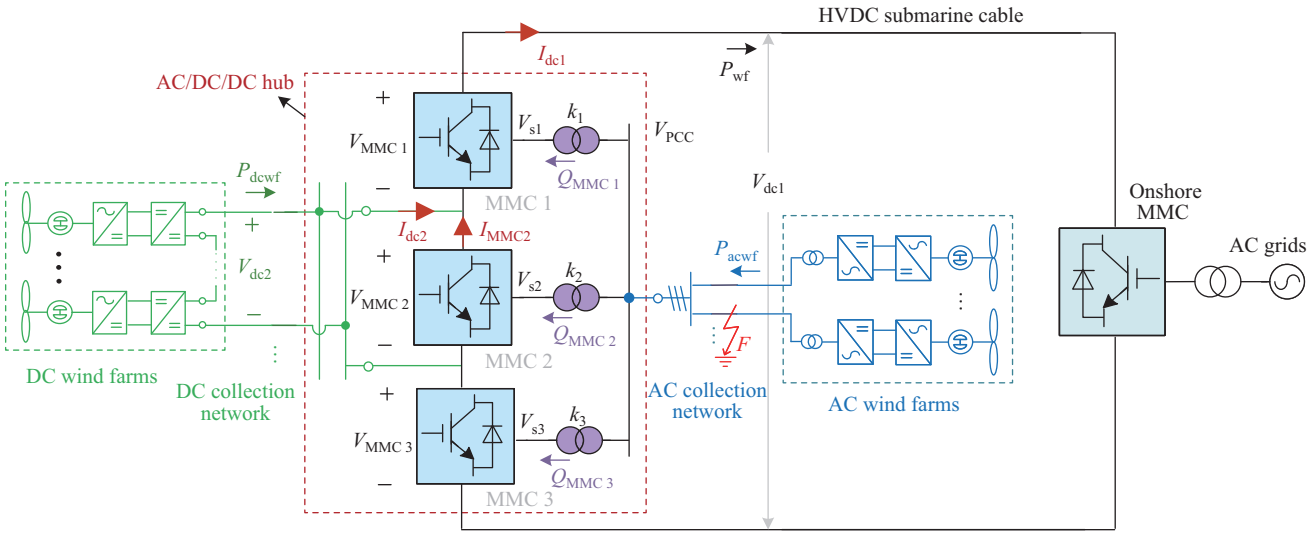

Fig. 1. Topology of the offshore wind integration system using hybrid AC/DC collection and HVDC transmission.

V_{MMC3}, respectively. The HVDC link and MVDC voltages are V_{dc1} and V_{dc2}, respectively. As shown in Fig. 1, the DC and AC voltages of the AC/DC/DC hub satisfy:

$$V_{\mathrm{dc1}} = V_{\mathrm{MMC1}} + V_{\mathrm{MMC2}} + V_{\mathrm{MMC3}} \tag{1}$$

$$m_1 V_{\mathrm{MMC1}} = \frac{2\sqrt{2}}{\sqrt{3}} V_{\mathrm{S1}},\ m_2 V_{\mathrm{MMC2}} = \frac{2\sqrt{2}}{\sqrt{3}} V_{\mathrm{S2}}$$
$$m_3 V_{\mathrm{MMC3}} = \frac{2\sqrt{2}}{\sqrt{3}} V_{\mathrm{S3}} \tag{2}$$

where V_{S1}, V_{S2} and V_{S3} are the AC side voltages of MMC1, MMC2 and MMC3, respectively. m_1, m_2 and m_3 are the AC modulation ratios of MMC1, MMC2 and MMC3, respectively. The range of modulation ratio m is generally $0.8 < m < 1$.

The relationship between the AC side voltage of the MMC and the PCC voltage is expressed as:

$$V_{\mathrm{S1}} = k_1 V_{\mathrm{PCC}}, V_{\mathrm{S2}} = k_2 V_{\mathrm{PCC}}, V_{\mathrm{S3}} = k_3 V_{\mathrm{PCC}} \tag{3}$$

where V_{PCC} is the voltage at PCC. k_1, k_2 and k_3 are the voltage ratios of the high voltage (HV) side windings to the low voltage (LV) side windings of the interfacing transformers of MMC1, MMC2 and MMC3, respectively. The configurations of MMC1 and MMC3 are identical. Their interfacing transformers are also of the same type. Therefore, $k_1 = k_3$. Additionally, their rated DC voltage levels are also the same.

Ignoring the operating power loss of DC collection submarine cable, V_{MMC2} is equal to V_{dc2}. Taking the power flow direction shown in Fig. 1 as the positive direction, the DC currents can be expressed as:

$$\begin{cases} I_{\mathrm{dc1}} = \dfrac{P_{\mathrm{wf}}}{V_{\mathrm{dc1}}} \\ I_{\mathrm{dc2}} = \dfrac{P_{\mathrm{dcwf}}}{V_{\mathrm{dc2}}} = \dfrac{P_{\mathrm{dcwf}}}{V_{\mathrm{MMC2}}} \\ I_{\mathrm{MMC2}} = I_{\mathrm{dc2}} - I_{\mathrm{dc1}} = \dfrac{P_{\mathrm{dcwf}}}{V_{\mathrm{MMC2}}} - \dfrac{P_{\mathrm{wf}}}{V_{\mathrm{dc1}}} \end{cases} \tag{4}$$

where I_{dc1} is the current of the HVDC submarine cables. I_{dc2} is the current of the DC collection network flowing through the AC/DC/DC hub. I_{MMC2} is the current of the DC side of MMC2. P_{wf} is the total power of the AC and DC wind farms.

To analyze the power characteristics and rated capacity of the AC/DC/DC hub, define the DC voltage ratio n between V_{dc2} and V_{dc1} as:

$$n = \frac{V_{\mathrm{dc2}}}{V_{\mathrm{dc1}}} = \frac{V_{\mathrm{MMC2}}}{V_{\mathrm{dc1}}},\ 0 < n < 1 \tag{5}$$

Define the active power ratio α between P_{dcwf} and P_{wf} as:

$$\alpha = \frac{P_{\mathrm{dcwf}}}{P_{\mathrm{wf}}}, 0 \le \alpha \le 1 \tag{6}$$

Based on (1)–(6), the power of each MMC can be calculated as follows. From (7), the operating power of MMC1 and MMC3 is related to P_{wf} and n. Moreover, P_{MMC1} and P_{MMC3} are always greater than 0, indicating that MMC1 and MMC3 always operate in rectifier conditions. Meanwhile, it can be seen in (8) that the operating power of MMC2 is related to P_{wf} and n, α. With different values of n and α, MMC2 can operate in the rectifier or inverter conditions.

$$\begin{aligned} P_{\mathrm{MMC1}} = P_{\mathrm{MMC3}} &= V_{\mathrm{MMC1}} I_{\mathrm{dc1}} = \frac{V_{\mathrm{dc1}} - V_{\mathrm{MMC2}}}{2} \cdot \frac{P_{\mathrm{wf}}}{V_{\mathrm{dc1}}} \\ &= \frac{1 - \frac{V_{\mathrm{MMC2}}}{V_{\mathrm{dc1}}}}{2} P_{\mathrm{wf}} = \frac{1-n}{2} P_{\mathrm{wf}} > 0 \end{aligned} \tag{7}$$

$$\begin{aligned} P_{\mathrm{MMC2}} &= V_{\mathrm{MMC2}} I_{\mathrm{MMC2}} = V_{\mathrm{MMC2}} (I_{\mathrm{dc1}} - I_{\mathrm{dc2}}) \\ &= V_{\mathrm{MMC2}} \left(\frac{P_{\mathrm{wf}}}{V_{\mathrm{dc1}}} - \frac{P_{\mathrm{dcwf}}}{V_{\mathrm{dc2}}} \right) = \frac{V_{\mathrm{MMC2}}}{V_{\mathrm{dc1}}} P_{\mathrm{wf}} - P_{\mathrm{dcwf}} \\ &= (n - \alpha) P_{\mathrm{wf}} \end{aligned} \tag{8}$$

where P_{MMC1}, P_{MMC2} and P_{MMC3} are the power of MMC1, MMC2 and MMC3, respectively.

Taking the two cases $n < \alpha$ and $n = \alpha$ as examples, the power directions of the AC/DC/DC hub are illustrated in Fig. 2. In Fig. 2(a), when $n < \alpha$, part of the power from the DC input port flowing through two conversion paths-DC/AC (MMC2) and AC/DC (MMC1 and MMC3), amounting to $|n - \alpha| P_{\mathrm{wf}}$. It is first rectified by MMC2, then inverted by MMC1 and MMC3. The remaining part, which is $P_{\mathrm{dcwf}} - |n - \alpha| P_{\mathrm{wf}}$, is transmitted directly to the DC output port through the DC side of MMC1 and MMC3. Directly transmitting power leads to lower power loss and higher transmission efficiency. Meanwhile, the power from the

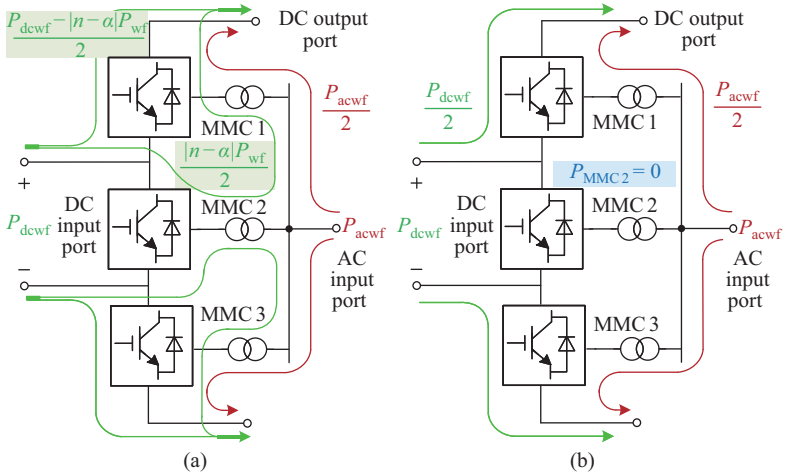

Fig. 2. AC and DC power directions in two situations: $n < \alpha$ and $n = \alpha$. (a) $n < \alpha$. (b) $n = \alpha$.

AC input port (P_{acwf}) is entirely transmitted to the AC side of MMC1 and MMC3 and then rectified to the DC output port.

In Fig. 2(b), when $n = \alpha$, accrording to (8), $P_{\mathrm{MMC2}} = 0$. In this case, the power from the DC input port (P_{dcwf}) is fully transferred to the DC output port via the DC side of MMC1 and MMC3. Compared to the conditions in Fig. 2(a), the transmission efficiency of the AC/DC/DC hub is higher due to the avoidance of the secondary power conversion process. While the power direction from the AC input port is the same as shown in Fig. 2(a).

III. Parameter Design of Hybrid AC/DC Collection and HVDC Transmission System

A. Power Ratio and DC Voltage Ratio Design

From (7) and (8), the operating power of MMCs is related to n and α. Summing up the operating power of MMC1, MMC2 and MMC3, the total operating power of the AC/DC/DC hub is calculated as:

$$P_{\mathrm{hub}} = \begin{cases} 2P_{\mathrm{MMC1}} + P_{\mathrm{MMC2}} = (1-\alpha)P_{\mathrm{wf}}, & n \geq \alpha \\ 2P_{\mathrm{MMC1}} - P_{\mathrm{MMC2}} = (1-2n+\alpha)P_{\mathrm{wf}}, & n \leq \alpha \end{cases} \tag{9}$$

where P_{hub} is the total operating power of the AC/DC/DC hub.

According to (9), the power ratio between P_{hub} and P_{wf} in different operation scenarios is plotted on the blue surface of Fig. 3. To visually compare the values of P_{hub} and P_{wf}, plot the yellow reference surface $P_{\mathrm{hub}}/P_{\mathrm{wf}} = 1$. The top of the reference surface indicates $P_{\mathrm{hub}} > P_{\mathrm{wf}}$, and the bottom indicates $P_{\mathrm{hub}} < P_{\mathrm{wf}}$. The above two surfaces intersect at the line $n = 0.5\alpha$.

1) When $n > 0.5\alpha$, $P_{\mathrm{hub}} < P_{\mathrm{wf}}$. The total operating power of the AC/DC/DC hub is lower than the power of the sending end MMC in the existing AC collection and HVDC transmission system (equals P_{wf}), which can effectively reduce the operation loss.

2) When $n < 0.5\alpha$, $P_{\mathrm{hub}} > P_{\mathrm{wf}}$. The demand for the rated capacity of the AC/DC/DC hub will increase. This results in a higher cost for the offshore converter station.

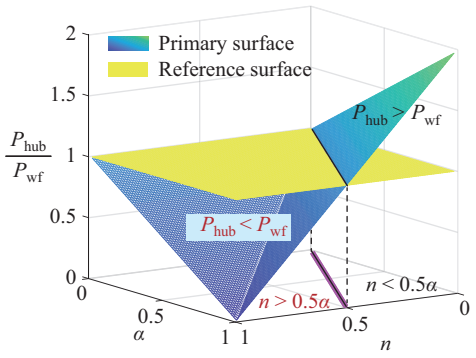

Fig. 3. Relationship of power ratio between P_{hub} and P_{wf} for different operating scenarios versus power ratios α and DC voltage ratios n.

3) For the same power transmission condition, the closer n and α are to 1, the smaller the total operating power of the AC/DC/DC hub is.

Therefore, there exists an optimal range for the DC voltage ratio n and the power ratio α:

$$n > 0.5\alpha \tag{10}$$

To further explore the optimal values of n and α, the effect of n and α on the operating power characteristics of each MMC is analyzed. Fig. 4 shows the plots of the operating power characteristics of MMCs under different operating scenarios based on (7) and (8).

Figure 4(a) shows the operating power characteristics of MMC1 (MMC3). It can be seen that the operating power of MMC1 (MMC3) is always greater than 0. Meanwhile, when the DC voltage ratio n increases, the operating power of MMC1 decreases, resulting in lower power loss. The operating power characteristics of MMC2 is depicted in Fig. 4(b). When $n > \alpha$, $P_{\mathrm{MMC2}} > 0$ and MMC2 operates in rectifier condition. When $n < \alpha$, $P_{\mathrm{MMC2}} < 0$ and MMC2 operates in inverter condition. When $n = \alpha$, $P_{\mathrm{MMC2}} = 0$. At the same time, the power loss of MMC2 is 0, and the power loss cost of MMC2 is greatly reduced.

In conclusion, the rated power and rated DC voltage of the AC/DC/DC hub should be designed as:

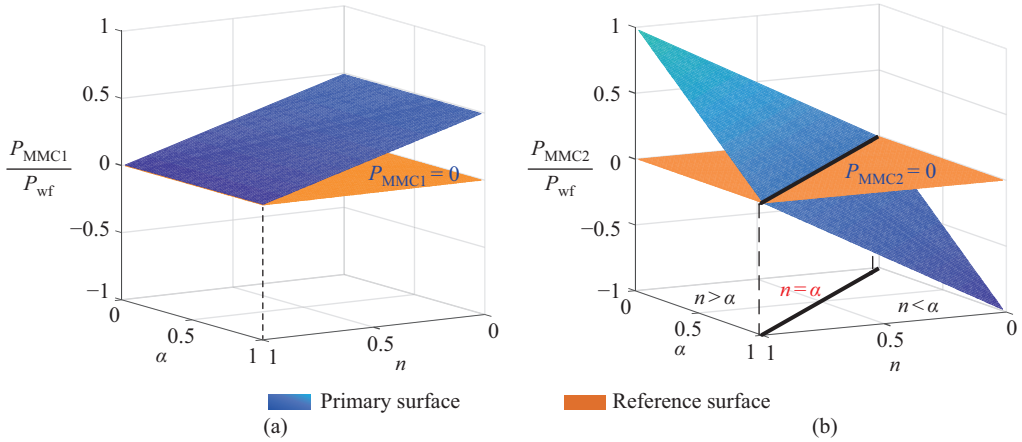

Fig. 4. Relationship of the MMC operating power under different operating scenarios with different power ratios α and DC voltage ratios n. (a) Power characteristics of MMC1. (b) Power characteristics of MMC2.

$$n = \alpha \tag{11}$$

Besides, n and α should take the maximum values in the feasible region. Take an example of a 2 GW offshore wind power integration scenario. The voltage of the HVDC submarine cable is ± 500 kV. According to existing DC voltage levels of the MVDC systems, the DC voltage level of the MVDC network is ± 100 kV [19]. Based on (11), the rated power of the offshore AC wind farms is 1600 MW, and the rated power of the offshore DC wind farms is 400 MW.

B. Requirement of AC/DC/DC Hub Capacity

The rated capacity of the AC/DC/DC hub should meet the system's full power operation demand. According to equation (7) and (11), the rated capacity of MMC1 and MMC3 should be designed by:

$$S_{\mathrm{MMC1}} = S_{\mathrm{MMC3}} = \frac{1-n}{2} P_{\mathrm{wf}N} = \frac{P_{\mathrm{wf}N} - P_{\mathrm{dcwfN}}}{2} \tag{12}$$

where S_{MMC1} and S_{MMC3} are the rated capacity of MMC1 and MMC3, respectively. $P_{\mathrm{wf}N}$ is the rated power of all wind farms. P_{dcwfN} is the rated power of DC wind farms.

When only the AC wind farms operate, $\alpha = 0$. According to equation (8), the operating power of MMC2 is expressed as follows. The operating power of MMC2 is greater than 0, indicating that it operates in rectifier conditions.

$$\begin{aligned} &P_{\mathrm{MMC2}} \\ &= (n-\alpha)P_{\mathrm{wf}} = nP_{\mathrm{acwfN}} = n(P_{\mathrm{wf}N} - P_{\mathrm{dcwfN}}) \\ &= n\left(\frac{1}{n}P_{\mathrm{dcwfN}} - P_{\mathrm{dcwfN}}\right) = (1-n)P_{\mathrm{dcwfN}} > 0 \end{aligned} \tag{13}$$

where P_{acwfN} is the rated power of AC wind farms.

When only the DC wind farms operate, $\alpha = 1$. The operating power of MMC2 is calculated as follows. It is obvious that the operating power of MMC2 is less than 0, indicating that it operates in inverter condition.

$$P_{\mathrm{MMC2}} = (n-\alpha)P_{\mathrm{wf}} = (n-1)P_{\mathrm{dcwfN}} < 0 \tag{14}$$

To cover all possible operating conditions, the rated capacity S_{MMC2} of MMC2 should be chosen as the maximum of the absolute values of (13) and (14). Since (13) and (14) are mutually opposite in sign, their absolute maximum values are the same. Therefore, the S_{MMC2} is designed as follows:

$$S_{\mathrm{MMC2}} = (1-n)P_{\mathrm{dcwfN}} \tag{15}$$

Therefore, the total rated capacity of the AC/DC/DC hub is calculated as follows. It is observed that the rated capacity of the AC/DC/DC hub is less than the total rated power of AC and DC wind farms.

$$\begin{aligned} S_{\mathrm{hub}} &= S_{\mathrm{MMC1}} + S_{\mathrm{MMC2}} + S_{\mathrm{MMC3}} \\ &= P_{\mathrm{wf}N} - nP_{\mathrm{dcwfN}} < P_{\mathrm{wf}N} \end{aligned} \tag{16}$$

where S_{hub} is the total rated capacity of the AC/DC/DC hub.

Based on the 2 GW integrated scenario described in the previous subsection and as indicated by (12), (15), and (16), the rated capacities are as follows: $S_{\mathrm{MMC1}} = S_{\mathrm{MMC3}} =$ 800 MVA, $S_{\mathrm{MMC2}} = 320$ MVA, and $S_{\mathrm{hub}} = 1920$ MVA.

IV. Control Design of Hybrid AC/DC Collection and HVDC Transmission System

A. Type I Control

Based on (1)–(3), the relationship between the PCC voltage of AC wind farms and the DC voltages is expressed in (17). It is indicated that an alternative way is to control the PCC voltage of AC wind farms by V_{MMC1} and V_{MMC3}. The onshore MMC station regulates V_{dc1} with DC voltage control, providing a stable DC voltage (V_{dc1}) for the AC/DC/DC hub. Therefore, MMC2 can be used to regulate the DC voltage V_{dc2} to integrate with DC wind farms, while MMC1 and MMC3 operate in grid forming (GFM) mode.

$$V_{\mathrm{MMC1}} + V_{\mathrm{MMC3}} = \frac{4\sqrt{6}k_1}{3m_1} V_{\mathrm{PCC}} = V_{\mathrm{dc1}} - V_{\mathrm{MMC2}} \tag{17}$$

Figure 5 depicts the control diagrams of MMC1-MMC3. In Fig. 5, V_d and V_q are the dq-axis components of the PCC voltage. I_d and I_q are the dq-axis components of the AC current of MMCs. V_{dc} is the DC voltage of MMCs. Q is the reactive power of MMC. m_d and m_q are the dq-axis components of the AC modulation ratio of MMCs. L is the sum of the transformer inductance and the arm inductance. f and ω are the frequency and angular frequency of the V_{PCC}, respectively. θ is the phase-angle reference of the trigger pulse.

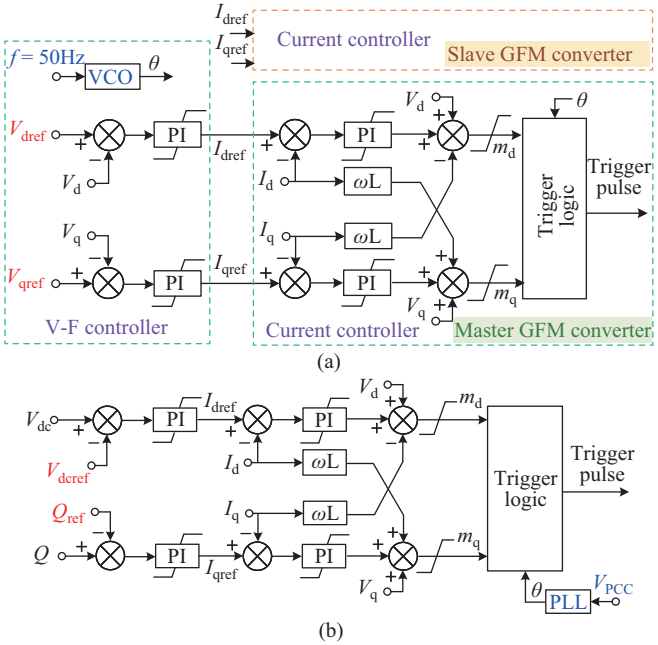

Fig. 5. Control diagrams of MMC1-MMC3. (a) GFM control of MMC1 and MMC3. (b) DC voltage control of MMC2.

To facilitate the calculation and analysis, all control parameters are per-unit values. The subscript 'ref' indicates the reference value of the corresponding parameter.

Figure 5(a) shows the GFM control of MMC1 and MMC3. Since MMC1 and MMC3 share the same AC bus, one MMC will be a master GFM converter, while the other MMC operates as a slave GFM converter, following the output of the V-F controller. In Fig. 5(b), the target of DC voltage control is to maintain V_{dc2} stable. Q_{ref} is set based on the system's

reactive power demand. The surplus reactive power can be shared by the MMC operating with GFM control.

B. Type II Control

Referring to (1)–(3), the relationship between the PCC voltage and the DC voltages can be expressed as:

$$V_{\mathrm{MMC2}} = \frac{2\sqrt{6}k_2}{3m_2}V_{\mathrm{PCC}} = V_{\mathrm{dc1}} - (V_{\mathrm{MMC1}} + V_{\mathrm{MMC3}}) \quad (18)$$

To integrate with AC wind farms, an intuitive way is to adopt GFM control for MMC2. According to (18), the effectiveness of grid forming control (V_{PCC}) relies on the stability of the DC voltages of V_{MMC1} and V_{MMC3}. Thus, MMC1 and MMC3 are designed to control their respective DC voltages. MMC2 is designed to control the AC voltage and frequency at PCC to provide a stable voltage for the AC wind farms.

V. Economic Evaluation

To further evaluate the economics of the proposed topology in this paper, this section compares the cost of the existing AC collection and MMC-HVDC transmission system (Scheme I) with the hybrid AC/DC collection and HVDC transmission system (Scheme II). The topologies of the two schemes are shown in Fig. 6.

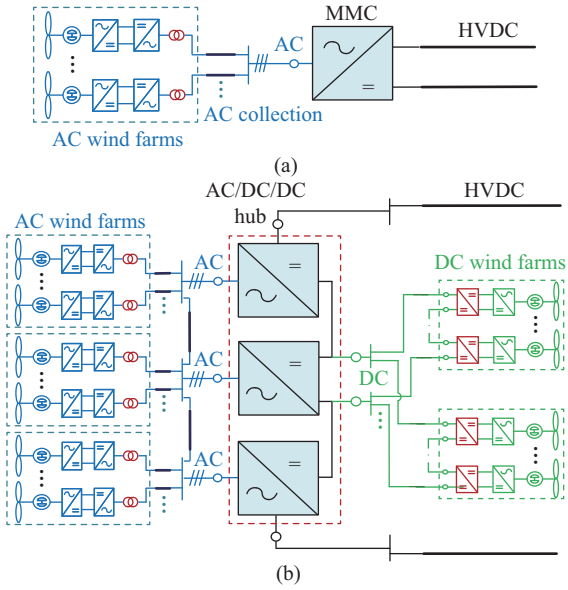

Fig. 6. Comparison of offshore wind power integrated topologies. (a) Topology of AC collection and MMC-HVDC transmission (Scheme I). (b) Topology of the proposed approach (Scheme II).

As shown in Fig. 6, the differences in the components cost of the two schemes include the offshore wind farms, the collection submarine cables and the offshore converter station. In Fig. 6(a), Scheme I includes AC wind farms, AC collection cables, and MMC station. In Fig. 6(b), Scheme II includes AC and DC wind farms, AC and DC collection cables, and the AC/DC/DC hub.

In addition, according to the analysis above, the operating power loss of the AC/DC/DC hub for the same transmission capacity is significantly less than the required MMC rating. Therefore, the power loss cost will also be considered.

The cost of wind turbines, collection cables, offshore converter station and operating power loss for two large-scale offshore wind power integration topologies are calculated as follows.

A. Wind Turbines

The offshore wind farms of the two schemes use PMSG with a capacity of 10 MW. The cost of PMSG WTs is:

$$C_{\mathrm{OWF}} = n_w C_w P_N \quad (19)$$

where C_{OWF} is the total cost of WTs. n_w is the number of turbines. C_w is the per-kilowatt cost of a single turbine. P_N is the installed capacity of a single turbine. Including the step-up transformer inside the turbine, a 66 kV AC turbine costs CNY 3950 per kW, and a ± 20 kV DC turbine costs CNY 4200 per kW [3].

B. Collection Cables

The initial investment cost of the collection cables is:

$$C_{\mathrm{cab}} = n_1 l_1 C_{\mathrm{cab\_AC}} + n_2 l_2 C_{\mathrm{cab\_DC}} \quad (20)$$

where C_{cab} is the total cost of collection cables. $C_{\mathrm{cab\_AC}}$ is the per-kilometer cost of AC collection cables. $C_{\mathrm{cab\_DC}}$ is the per-kilometer cost of DC collection cables. n_1 and n_2 are the circuit numbers of AC and DC collection cables, respectively. l_1 and l_2 are the cable lengths from the AC and DC wind farms to the AC/DC/DC hub, respectively. In Scheme I, $l_1 =$ 20 km. In Scheme II, $l_1 =$ 10 km and $l_2 =$ 40 km.

Given that a 66 kV AC collection cable can connect six 10 MW WTs, in Scheme I, $n_1 =$ 34 and $n_2 =$ 0. While in Scheme II, $n_1 =$ 27 and $n_2 =$ 2. The cost of 66 kV AC cables is CNY 2.6 m per km. And the cost of ± 100 kV DC cables is CNY 2.2 m per km [20].

C. Offshore Converter Station

The cost of the offshore converter station is [20]:

$$C_{\mathrm{con}} = B_{\mathrm{c}} + [1 + f_{\mathrm{c}}(N_T - 2)]V_{\mathrm{c}}S_N \quad (21)$$

where C_{con} is the total cost of the offshore converter station. B_{c} and V_{c} are the base cost (CNY 225 m) and variable cost (CNY 0.981 m per MVA) for offshore platforms, respectively. f_{c} is the cost factor of converter number per platform, which is 0.2. N_T is the transformer number per converter, which is taken as 1. S_N is the converter's rated capacity. In Scheme I, $S_N = S_{\mathrm{wf}N} =$ 2000 MVA. Meanwhile, in Scheme II, $S_N = S_{\mathrm{hub}} =$ 1920 MVA.

D. Operating Power Loss

The cost of operating power loss is usually calculated in terms of annual value (annual loss cost). The differences in operating power loss between the two schemes are mainly in the offshore converter station and the collection cables.

The annual loss cost of the offshore converter station is:

$$C_{\mathrm{los\_year}} = k_s P T C_{\mathrm{ele}} \quad (22)$$

where $C_{\text{los\_year}}$ is the annual loss cost of the offshore converter station. k_s is the loss cost coefficient of the offshore converter station, which is selected as 0.8% [21]. P is the operating power of the converter. T is the annual utilization hours of offshore wind farms, which is selected as 4000 h [22]. C_{ele} is the cost of electricity price, which is taken as CNY 0.45 per kWh [20].

The annual loss cost of the AC collection cables is:

$$C_{\text{los\_ac}} = P_{\text{los\_ac}} T C_{\text{ele}} = 3 \times \left(\frac{P_{\text{acwf}}}{\sqrt{3} V_{\text{PCC}} \cos\varphi} \right)^2 R_{\text{ac}} l_1 T C_{\text{ele}} \quad (23)$$

where $C_{\text{los\_ac}}$ is the annual loss cost of the AC collection cables. $P_{\text{los\_ac}}$ is the operating power loss of the AC collection cables. $\cos\varphi$ is the power factor with an approximate value of 0.95. R_{ac} is the resistance of the AC collection cables per unit length, which is taken as 0.0496 Ω/km [3].

The annual loss cost of the DC collection cables is:

$$C_{\text{los\_dc}} = P_{\text{los\_dc}} T C_{\text{ele}} = 2 \times \left(\frac{P_{\text{dcwf}}}{V_{\text{dc2}}} \right)^2 R_{\text{dc}} l_2 T C_{\text{ele}} \quad (24)$$

where $C_{\text{los\_dc}}$ is the annual loss cost of the DC collection cables. $P_{\text{los\_dc}}$ is the operating power loss of the DC collection cables. R_{dc} is the resistance of the DC collection cables per unit length, taken as 0.0137 Ω/km [20].

Assuming that the life cycle of the large-scale offshore wind power integrated project is 20 years, and the annual interest rate is 5% [23], the operating power loss cost after discounting to the present value is:

$$C_{\text{los}} = \frac{(1+r)^t - 1}{r(1+r)^t} C_{\text{los\_year}} \quad (25)$$

where C_{los} is the operating power loss cost. r is the annual interest rate taken as 0.05. t is the life cycle, which equals 20.

In the economic analysis, taking the 2 GW offshore wind power integration scenario as an example, the results are depicted in Table I. It can be seen from Table I that the cost of Scheme I is higher than that of Scheme II by CNY 1224 m. In conclusion, the proposed integration concept can improve the economic efficiency of the overall integration system and is promising for large-scale offshore wind power integration. It should be noted that the costs of HVDC transmission cables and onshore converter stations of the two schemes are the same. And they are not given in Table I.

VI. Simulation Verification

To verify the technical feasibility of the proposed topology, a simulation model of the hybrid AC/DC collection and HVDC transmission system shown in Fig. 1 is built in PSCAD/EMTDC. The parameters of the model are given in Table II.

The simulation example's AC and DC wind farms are rated at 1600 MW and 400 MW, respectively. The DC voltage ratings are ±100 kV, ±500 kV, and the AC voltage V_{PCC} is 66 kV. The AC collection submarine cables are modeled using a π-equivalent circuit. The DC submarine cables are equated by resistances [24].

TABLE II
Parameters of the Simulation Model

Parameters		Value
AC wind farms	Power rating (MW)	1600
	Rated AC voltage (kV)	66
	Frequency (Hz)	50
	AC collection cable length (km)	270
DC wind farms	Power rating (MW)	400
	Rated DC voltage (kV)	± 100
	DC collection cable length (km)	80
HVDC transmission	Power rating (MW)	2000
	Rated DC voltage (kV)	± 500
MMC1 & MMC3	Rated capacity (MVA)	800
	Rated DC voltage (kV)	400
	Number of SM per arm	200
	SM capacitance (mF)	13
	Arm inductance (mH)	60
	Interfacing transformer voltage ratio (kV)	66/210
MMC2	Rated capacity (MVA)	400
	Rated DC voltage (kV)	± 100
	Number of SM per arm	100
	SM capacitance (mF)	13
	Arm inductance (mH)	30
	Interfacing transformer voltage ratio (kV)	66/105

A. Comparison of the Two Types of Control

1) Performance Under Normal Operation

In Fig. 7, the simulation and comparison are carried out between type I and type II control methods of the proposed system under normal operation. The left column shows the simulation results of the type I control, and the right column shows the type II control.

As shown in Fig. 7(a), the operating power of the AC and DC wind farms are stepped linearly from 0 to respective rated values (1600 MW and 400 MW) within 5 s∼6 s. During 6 s∼9 s, the system operates normally with a total power (P_{wf}) of 2000 MW.

TABLE I
Cost Comparison of Two Large-scale Offshore Wind Integration Schemes with a Capacity of 2 GW

Topology	Comparison objects	Parameters	Cost/CNY
AC collection and MMC-HVDC transmission	Wind turbines	$P_{\text{acwf}} = 2000$ MW	7900 m
	Collection cables	$V_{\text{PCC}} = 66$ kV	1768 m
	Offshore converter station	$S_{\text{MMC}} = 2000$ MVA	1795 m
	Operating power loss	$P_{\text{MMC}} = 2000$ MW	1025 m
	Total	–	12488 m
Hybrid AC/DC collection and HVDC transmission	Wind turbines	$P_{\text{dcwf}} = 400$ MW, $P_{\text{acwf}} = 1600$ MW	8000 m
	Collection cables	$V_{\text{dc2}} = \pm 100$ kV, $V_{\text{PCC}} = 66$ kV	878 m
	Offshore converter station	$S_{\text{hub}} = 1920$ MVA	1732 m
	Operating power loss	$P_{\text{hub}} = 1600$ MW	654 m
	Total	–	11264 m

Figure 7(b) presents the DC voltages of V_{dc1} and V_{dc2}. Since there is power loss in the HVDC submarine cables, it can be observed that V_{dc1} is slightly higher than the reference voltage (1000 kV) controlled by the onshore MMC station. In type I control, since the MMC2 is designed to control the DC voltage, $V_{\mathrm{MMC2}} = 1$ p.u. (200 kV), $V_{\mathrm{MMC1}} = V_{\mathrm{MMC3}} =$ 404 kV and $V_{\mathrm{dc1}} = 1008$ kV. In type II control, since the MMC1 and MMC3 are designed to control their respective DC voltages, $V_{\mathrm{MMC1}} = V_{\mathrm{MMC3}} = 1$ p.u. (400 kV). Besides, $V_{\mathrm{dc2}} = 208$ kV and $V_{\mathrm{dc1}} = 1008$ kV. This indicates that the DC voltages are well controlled by both control methods.

Figure 7(c) shows the active power of MMCs. P_{MMC1} and P_{MMC3} are ramped from 0 MW at 5 s to about 800 MW at 6 s, while P_{MMC2} remains nearly at 0 MW. It indicates that under normal operation, the total power of the AC/DC/DC hub (P_{hub}) with only 1600 MW can provide 2000 MW power for the onshore AC grids (P_{wf}), which validates the advantages of power characteristics of the AC/DC/DC hub.

Figure 7(d) depicts the reactive power of MMCs. The reactive power absorbed by the inductance of the AC collection cables increases when the operating power of the AC wind farms increases at 5 s∼6 s, resulting in a decrease in the total reactive power of MMCs (Q_{hub}). The distribution of Q_{hub} is related to the control strategy adopted by each MMC. Under the two proposed control methods, it is regulated by the MMC that adopted the GFM control. In type I control, Q_{hub} is regulated equally by MMC1 and MMC3. In type II control, Q_{hub} is exclusively regulated by MMC2.

Figure 7(e) shows the *dq* axis components (V_{PCCd} and V_{PCCq}) of the PCC voltage. It can be seen that V_{PCCd} and V_{PCCq} are always maintained at 1 p.u. (66 kV) and 0, respectively. Fig. 7(f) shows the frequency at the PCC, which maintains steady at 50 Hz. These observations validate that the GFM control of MMC effectively stabilizes the PCC voltage and frequency.

The simulation results in Fig. 7 validate the effectiveness of the type I and type II control. Both control strategies can provide sound grid-forming capabilities for AC and DC wind farms.

2) *Performance Under AC Short-circuit Fault*

Figure 8 shows the simulation results of an AC short-circuit fault (F) occurring at the terminal of a string of AC wind turbines as illustrated in Fig. 1. At 7.5 s, an AC short-circuit fault occurs, and the circuit breaker disconnects 0.1 s later. Fig. 8(a) shows the operating active power of AC wind farms (P_{acwf}). It can be observed that after the circuit breaker disconnects, type I control allows P_{acwf} to stabilize more quickly compared to type II control. Fig. 8(b) is the RMS value of PCC voltage. Similarly, the PCC voltage under type I control stabilizes more quickly. Fig. 8(c) presents the DC voltages V_{dc1} and V_{dc2}. The DC voltage remains stable under the two types of control.

In conclusion, type I control shows a minor improvement in the AC collection network due to the larger capacity of the GFM MMCs. In the following sections, the performance using the type I control will be studied as an example.

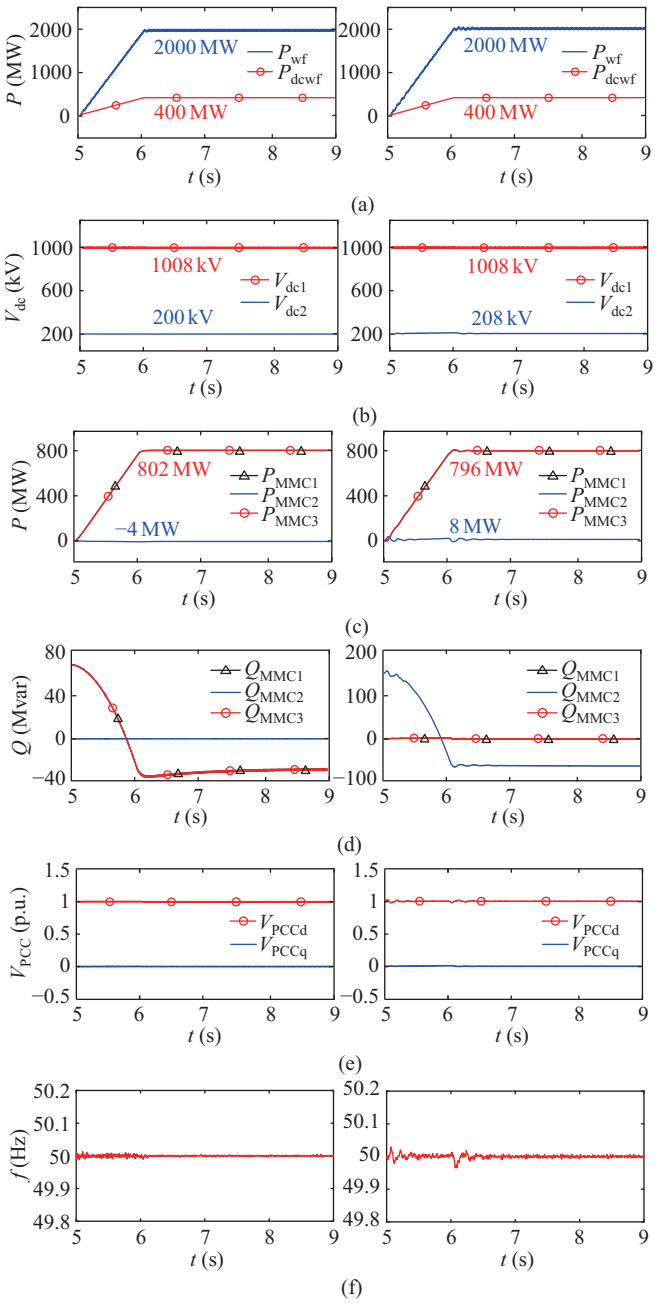

Fig. 7. Simulation results of type I and type II control-based systems under normal operation. (a) Active power of wind farms. (b) DC voltage. (c) Active power of MMCs. (d) Reactive power of MMCs. (e) PCC voltage. (f) PCC frequency.

B. *Performance Under Power Curtailment*

Figure 9 shows the simulation results of the proposed system under power curtailment. The DC power P_{wf} and P_{dcwf} are shown in Fig. 9(a). Initially, the system was stable and under normal operation. From 6.5 s to 7 s, P_{wf} decreases from 2000 MW to 1500 MW, and P_{dcwf} reduces in equal proportion from 400 MW to 300 MW. It can be noticed that $n = \alpha$ from 5 s to 8 s, marked with a blue area in Fig. 9(a). Meanwhile, $P_{\mathrm{MMC2}} = 0$ as shown in Fig. 9(c). Therefore, even if the system operates at abnormal operating conditions, it can still satisfy $P_{\mathrm{MMC2}} = 0$, as long as P_{wf} and P_{dcwf} vary in equal

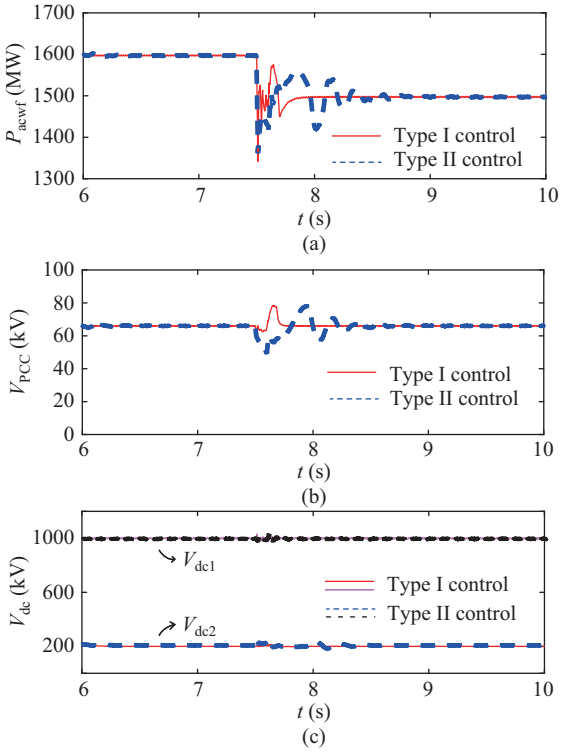

Fig. 8. Simulation results of transient AC short-circuit fault occurring at the terminal of a string of AC WTs. (a) Active power of AC wind farms. (b) RMS value of PCC voltage. (c) DC voltage.

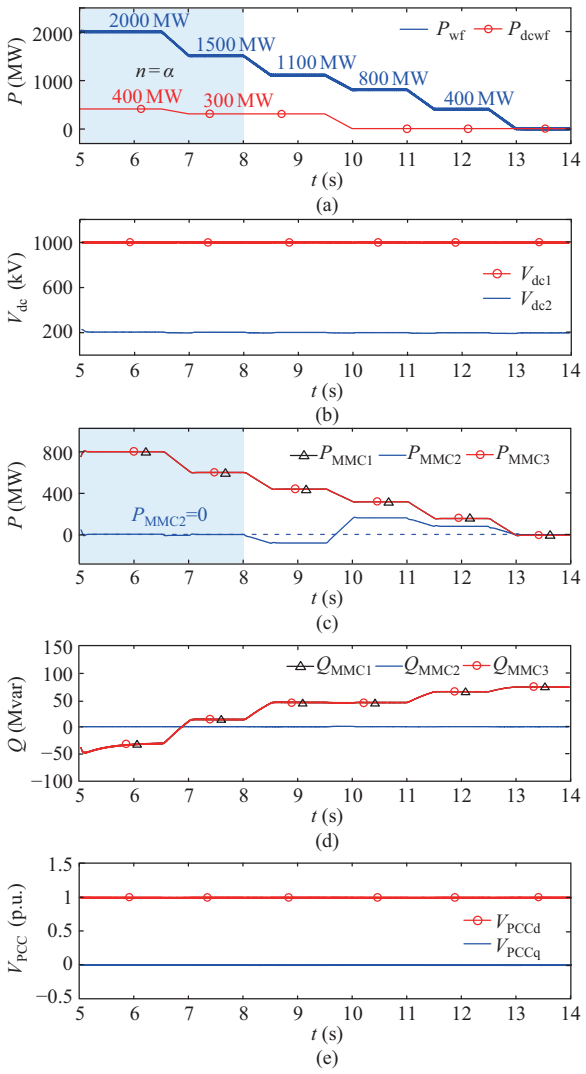

Fig. 9. Simulation results of the proposed system under power curtailment. (a) Active power of wind farms. (b) DC voltage. (c) Active power of MMCs. (d) Reactive power of MMCs. (e) The *dq* axis components of PCC voltage.

proportions (satisfying $n = \alpha$). In addition, P_{dcwf} decreases from 300 MW to 0 MW during 9.5 s∼10 s. During 8 s∼13 s, P_{wf} reduces gradually from 1500 MW to 0 MW. Meanwhile, the DC power changes disproportionately, resulting in P_{MMC2} not equal to 0.

It can be seen from Fig. 9(b) and (e) that when the operating power of the wind farms varies, both the DC and AC voltage are maintained at the rated value. In Fig. 9(d), since the system adopts the type I control as an example, Q_{MMC2} remains at 0. The reactive power is equally shared between MMC1 and MMC3. Besides, with the decrease in the operating power of the AC wind farms, Q_{MMC1} and Q_{MMC3} increase.

Therefore, simulation results from Fig. 9 verify that the system can adapt to the whole power operation under significant wind power fluctuation.

C. Performance Under Single Type WF Operations

1) Only AC Wind Farms Are in Operation:

The power of AC WFs P_{acwf} stepped up from 0 to the rated value at 5 s ($P_{\mathrm{acwfN}} = 1600$ MW), while P_{dcwf} remains at 0. The DC powers P_{wf} and P_{dcwf} are shown in Fig. 10(a).

Figure 10(b) presents the DC voltages V_{dc1} (1007 kV) and V_{dc2} (207 kV). Since the MMC1 and MMC3 are designed to control their respective DC voltages, $V_{\mathrm{MMC1}} = V_{\mathrm{MMC3}} =$ 1 p.u. (400 kV).

As shown in Fig. 10(c), $P_{\mathrm{MMC1}} = P_{\mathrm{MMC3}} = 638$ MW and $P_{\mathrm{MMC2}} = 320$ MW, which is consistent with (13). Meanwhile, each MMC operates in rectifier conditions. Combining $Q_{\mathrm{MMC1}} = Q_{\mathrm{MMC3}} = -31$ Mvar and $Q_{\mathrm{MMC2}} = 0$ Mvar in Fig. 10(d), the rated capacity of the AC/DC/DC hub meets the demand of operating conditions when only AC wind farms are in operation.

In Fig. 10(e), the PCC voltage stabilizes at 1 p.u. (66 kV) by GFM control. Fig. 10(f) shows DC currents I_{dc1} and I_{dc2}. Since the power of the DC wind farms is 0, $I_{\mathrm{dc2}} = 0$. Besides, $I_{\mathrm{dc1}} = 1.6$ kA, within the capacity (2 kA) of the HVDC submarine cables.

2) Only DC Wind Farms Are in Operation

In Fig. 11(a), when only the DC wind farms are under normal operation during 6 s∼9 s, $P_{\mathrm{dcwf}} = P_{\mathrm{wf}} = 400$ MW. DC voltage V_{dc1} is 1002 kV and V_{dc2} is 202 kV, as shown in Fig. 11(b). Compared with the DC voltages in Fig. 10(b), the voltage drop between the V_{dc1} and the reference value (1000 kV) controlled by the onshore MMC station is lower, which is caused by the decrease of the operating power of the HVDC submarine cables.

Figure 11(c) depicts the active power of MMCs. From 6 s to 9 s, $P_{\mathrm{MMC1}} = P_{\mathrm{MMC3}} = 159$ MW and $P_{\mathrm{MMC2}} = -318$ MW, which can be consistent with equation (14). In this case, MMC2 operates in inverter condition. In Fig. 11(d),

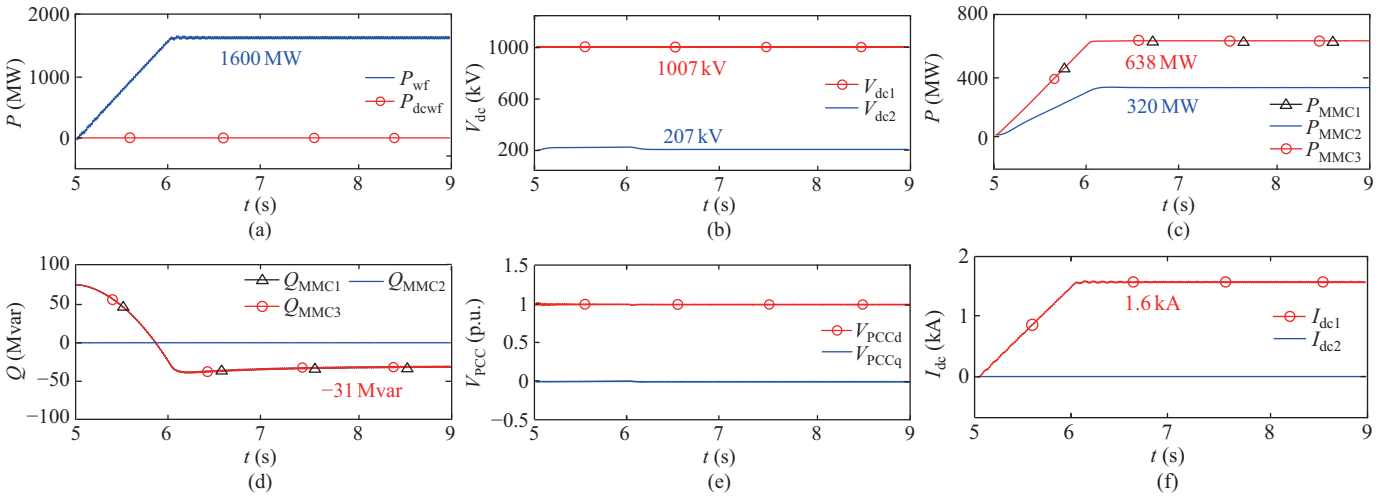

Fig. 10. Simulation results of the proposed system when only AC wind farms are operating. (a) Active power of wind farms. (b) DC voltage. (c) Active power of MMCs. (d) Reactive power of MMCs. (e) The *dq* axis components of PCC voltage. (f) DC current.

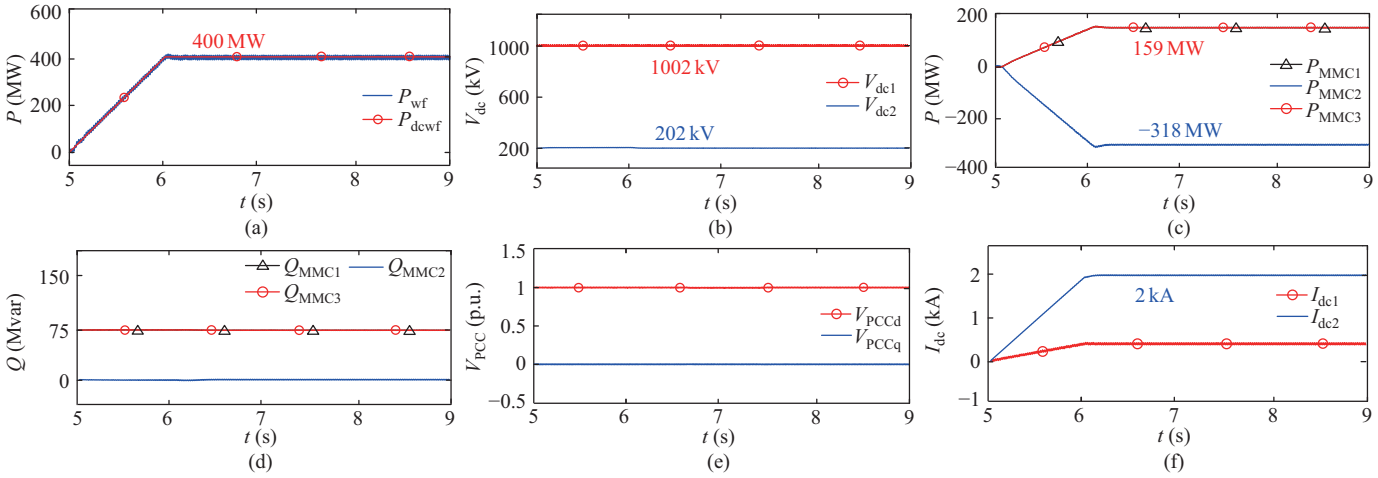

Fig. 11. Simulation results of the proposed system when only DC wind farms are operating. (a) Active power of wind farms. (b) DC voltage. (c) Active power of MMCs. (d) Reactive power of MMCs. (e) The *dq* axis components of PCC voltage. (f) DC current.

during 6 s∼9 s, $Q_{\mathrm{MMC2}} = 0$ Mvar and $Q_{\mathrm{MMC1}} = Q_{\mathrm{MMC3}} =$ 75 Mvar. The rated capacity of the AC/DC/DC hub also satisfies operating conditions when only DC wind farms operate. From Fig. 11(b) and (e), it can be observed that both the AC and DC voltages are well controlled at the rated values. Meanwhile, both the DC currents I_{dc1} and I_{dc2} are also within the current capacity (2 kA) of the DC submarine cables, as shown in Fig. 11(f).

VII. Conclusion

The paper proposes a hybrid AC/DC collection and HVDC transmission concept for large-scale offshore wind power, featuring a three-terminal hybrid AC/DC/DC hub. The system's operating characteristics are analyzed, indicating that partial or even full power of the DC wind farms can be transmitted directly through the DC side of MMC1 and MMC3. Thus, the AC/DC/DC hub can have a lower operating power and higher transmission efficiency.

A parameter design method for the AC/DC/DC hub is introduced. It is demonstrated that when the DC voltage ratio n equals the power ratio α, the operating power of the AC/DC/DC hub is minimized. This approach results in reduced operating power loss and lower investment costs. In a case study of a 2 GW offshore wind power integration scenario, the minimum operating power of the AC/DC/DC hub is only 1600 MW as the offshore wind farms operate at their rated capacity. Economic analysis indicates that the total cost of the proposed system is reduced by CNY 1224 m compared with existing MMC-HVDC integration technologies.

Two AC/DC/DC hub control strategies are proposed and validated. Simulation results confirm the technical feasibility of the proposed system, validating its adaptability across the full power operating range. However, the AC/DC fault management strategies for both onshore and offshore faults need further investigation. Moreover, the scaled-down experiments need to be performed in future studies.

References

[1] Global Wind Energy Council. (2023, Jun.). GWEC Global Wind Report

2023. [Online]. Available: https://www.enertechnos.com/news/press-releases/gwec-global-wind-report-2023/.
[2] W. Xiang, S. Z. Yang, G. P. Adam, H. B. Zhang, W. P. Zuo, and J. Y. Wen, "DC fault protection algorithms of MMC-HVDC grids: fault analysis, methodologies, experimental validations, and future trends," *IEEE Transactions on Power Electronics*, vol. 36, no. 10, pp. 11245–11264, Oct. 2021.
[3] J. Lyu, W. J. Yang, W. Huang, H. Pang, M. Kong, Y. X. Yang, and W. W. Zhang, "Techno-economic of 66 kV AC connection solution for offshore wind power," *Electric Power*, vol. 53, no. 7, pp. 72–79, Jul. 2020.
[4] J. Dakic, M. Cheah-Mane, O. Gomis-Bellmunt, and E. Prieto-Araujo, "HVAC transmission system for offshore wind power plants including mid-cable reactive power compensation: optimal design and comparison to VSC-HVDC transmission," *IEEE Transactions on Power Delivery*, vol. 36, no. 5, pp. 2814–2824, Oct. 2021.
[5] P. Lakshmanan, R. J. Sun, and J. Liang, "Electrical collection systems for offshore wind farms: a review," *CSEE Journal of Power and Energy Systems*, vol. 7, no. 5, pp. 1078–1092, Sep. 2021.
[6] L. Li, B. B. Li, Z. Y. Wang, M. Yang, and D. G. Xu, "Monopolar symmetrical DC-DC converter for all DC offshore wind farms," *IEEE Transactions on Power Electronics*, vol. 37, no. 4, pp. 4275–4287, Apr. 2022.
[7] Z. H. Zhang, P. Kou, Y. H. Zhang, and D. L. Liang, "Coordinated predictive control of offshore DC collection grid and wind turbines for frequency response: a scheme without secondary frequency drop," *IEEE Transactions on Sustainable Energy*, vol. 14, no. 3, pp. 1488–1503, Jul. 2023.
[8] M. Pape and M. Kazerani, "An offshore wind farm with DC collection system featuring differential power processing," *IEEE Transactions on Energy Conversion*, vol. 35, no. 1, pp. 222–236, Mar. 2020.
[9] J. D. Páez, D. Frey, J. Maneiro, S. Bacha, and P. Dworakowski, "Overview of DC-DC converters dedicated to HVdc grids," *IEEE Transactions on Power Delivery*, vol. 34, no. 1, pp. 119–128, Feb. 2019.
[10] M. Pape and M. Kazerani, "A generic power converter sizing framework for series-connected DC offshore wind farms," *IEEE Transactions on Power Electronics*, vol. 37, no. 2, pp. 2307–2320, Feb. 2022.
[11] X. D. Zhao, B. B. Li, B. X. Zhang, and D. G. Xu, "A high-power step-up DC/DC converter dedicated to DC offshore wind farms," *IEEE Transactions on Power Electronics*, vol. 37, no. 1, pp. 65–69, Jan. 2022.
[12] A. Erat and A. M. Vural, "DC/DC modular multilevel converters for HVDC interconnection: a comprehensive review," *International Transactions on Electrical Energy Systems*, vol. 2022, pp. 2687243, Sep. 2022.
[13] P. F, Hu, R. Yin, B. Z. Wei, Y. J. Luo, and F. Blaabjerg, "Modular isolated LLC DC/DC conversion system for offshore wind farm collection and integration," *IEEE Journal of Emerging and Selected Topics in Power Electronics*, vol. 9, no. 6, pp. 6713–6725, Dec. 2021.
[14] W. Liao, Q. W. Wu, H. S. Cui, S. Huang, Y. S. Gong, and B. Zhou, "Model predictive control based coordinated voltage control for offshore radial DC-connected wind farms," *Journal of Modern Power Systems and Clean Energy*, vol. 11, no. 1, pp. 280–289, Jan. 2023.
[15] B. B. Li, J. Y. Liu, Z. Y. Wang, S. X. Zhang, and D. G. Xu, "Modular high-power DC-DC converter for MVDC renewable energy collection systems," *IEEE Transactions on Industrial Electronics*, vol. 68, no. 7, pp. 5875–5886, Jul. 2021.
[16] M. Y. Guan, "A series-connected offshore wind farm based on modular dual-active-bridge (DAB) isolated DC-DC converter," *IEEE Transactions on Energy Conversion*, vol. 34, no. 3, pp. 1422–1431, Sep. 2019.
[17] F. An, B. Zhao, B. Cui, and R. H. Bai, "Multi-functional DC collector for future All-DC offshore wind power system: concept, scheme, and implement," *IEEE Transactions on Industrial Electronics*, vol. 69, no. 8, pp. 8134–8145, Aug. 2022.
[18] F. An, B. Zhao, B. Cui, Y. S. Chen, L. Qu, Z. Q. Yu, and R. Zeng, "Selective virtual synthetic vector embedding for full-range current harmonic suppression of the DC collector," *IEEE Transactions on Power Electronics*, vol. 38, no. 2, pp. 2577–2588, Feb. 2023.
[19] CIGRE Working Group 31 of Study Committee C6. (2020, Feb.). Medium voltage direct current (MVDC) grid feasibility study [Online]. Available: https://electra.cigre.org/309-april-2020/
[20] X. Xiang, S. Y. Fan, Y. J. Gu, W. L. Ming, J. Z. Wu, W. H. Li, X. N. He, and T. C. Green, "Comparison of cost-effective distances for LFAC with HVAC and HVDC in their connections for offshore and remote onshore wind energy," *CSEE Journal of Power and Energy Systems*, vol. 7, no. 5, pp. 954–975, Sep. 2021.
[21] R. Li and L. Xu, "A unidirectional hybrid HVDC transmission system based on diode rectifier and full-bridge MMC," *IEEE Journal of Emerging and Selected Topics in Power Electronics*, vol. 9, no. 6, pp. 6974–6984, Dec. 2021.
[22] X. W. Shen, Q. W. Wu, H. C. Zhang, and L. M. Wang, "Optimal planning for electrical collector system of offshore wind farm with double-sided ring topology," *IEEE Transactions on Sustainable Energy*, vol. 14, no. 3, pp. 1624–1633, Jul. 2023.
[23] G. Abeynayake, T. Van Acker, D. Van Hertem, and J. Liang, "Analytical model for availability assessment of large-scale offshore wind farms including their collector system," *IEEE Transactions on Sustainable Energy*, vol. 12, no. 4, pp. 1974–1983, Oct. 2021.
[24] D. T. Feng, J. H. Xia, X. B. Li, X. L. Xiong and C. Y. Zhao, "Offshore low-frequency AC transmission system based on back to back current source converters," *CSEE Journal of Power and Energy Systems*, doi: 10.17775/CSEEJPES.2022.03240.

Wang Xiang received his B.Eng. and Ph.D. degrees both in Electrical Engineering from Huazhong University of Science and Technology (HUST), China in 2012 and 2017 respectively. He was a visiting Phd student at the University of Aberdeen and the University of Strathclyde in 2014 and 2016 respectively. He was with the University of Strathclyde from 2018 to 2021. Currently, he is a Professor at School of Electrical and Electronics Engineering, Huazhong University of Science and Technology, China. His main research interests include MMC-HVDC, high power DC/DC converters, DC grids and offshore wind power integration.

Rui Tu received the B.S. degree in Electrical Engineering from North China Electric Power University, Beijing, China, in 2023. She is currently working toward the Ph.D. degree in Electrical Engineering at Huazhong University of Science and Technology, Wuhan, China. Her research interests include MMC-HVDC and offshore wind power integration.

Mingyu Han received the B.S. degree in Electrical Engineering from South China University of Technology, Guangzhou, China, in 2020, and the M.S. degree from Huazhong University of Science and Technology, Wuhan, China, in 2023. His research interests include MMC-HVDC and offshore wind power integration.

Jinyu Wen received his B.Eng. and Ph.D. degrees all in Electrical Engineering from Huazhong University of Science and Technology (HUST), Wuhan, China, in 1992 and 1998, respectively. He was a visiting student from 1996 to 1997 and research fellow from 2002 to 2003 all at the University of Liverpool, UK, and a senior visiting researcher at the University of Texas at Arlington, USA in 2010. From 1998 to 2002 he was a director engineer in XJ Electric Co. Ltd. in China. In 2003 he joined the HUST and now is a Professor at HUST. His current research interests include renewable energy integration, energy storage application, DC grid, and power system operation and control.